Screened configuration interaction method for open-shell excited states applied to NV centers

W. Pfäffle,[1] D. Antonov,[2] J. Wrachtrup,[2] and G. Bester[1,3,*]

[1]*Institut für Physikalische Chemie, Universität Hamburg, Grindelallee 117, D-20146 Hamburg, Germany*
[2]*3. Physikalisches Institut, Universität Stuttgart, Pfaffenwaldring 57, D-70569 Stuttgart, Germany*
[3]*The Hamburg Centre for Ultrafast Imaging, Luruper Chaussee 149, D-22761 Hamburg, Germany*

We present a computational approach, based on density functional theory and screened configuration interaction, able to accurately treat highly correlated electron spins localized around semiconductor defects, typically occurring in the context of qubit implementations. The method is computationally not more demanding than a usual density functional theory calculation, which makes it suitable for the calculation of isolated defects, or defect complexes, typically requiring large simulation cells. We illustrate the approach by applying it to the three different charge states of the nitrogen vacancy defect in diamond and obtain very good agreement with experiment.

I. INTRODUCTION

Impurities in bulk or nanostructures are involved in a broad range of applications. A prominent example is the nitrogen-vacancy (NV) defect in diamond, consisting of a substitutional nitrogen atom with an adjacent vacancy, which can be used as a sensor of magnetic and electric fields with high sensitivity and spatial resolution [1–3], as solid-state quantum bit (qubit) [4,5], or as quantum probes for living cells [6,7]. All these examples require a clear understanding of the ground and the excited states and the ensuing optical properties of the defect center. The state-of-the-art approach for the calculation of excitation energies of defect states in semiconductors at the *ab initio* level is the GW approach in combination with the Bethe-Salpeter equation (GW-BSE) [8,9]. However, using this methodology provides for the NV center results, which do not agree with the experiment [10]. This is due to the fact that the standard GW-BSE approach does only take one configuration out of the three-fold ground state $^3A_2$ into account. GW-BSE considers single electron-hole excitations starting from this single ground-state configuration. As a consequence, the optically excited states belongs to a two-fold instead of the six-fold degenerate ^3E representation [8]. A method which takes several ground-state configurations into account is therefore required [8,10]. One possibility is to combine GW with a Hubbard model [10] and in a next step solving the Hamiltonian with exact diagonalization, which requires a fitting of the model Hamiltonian parameters to a GW calculation. Another method for defects in solids is based on the solution of an effective local Anderson impurity problem with a few strongly interacting localized orbitals using a truncated configuration interaction [11]. Another recent approach is a configuration interaction (CI) constrained random phase approximation (cRPA) approach [12], which leads to very accurate results but requires a computationally

very demanding screening. Very recently, Bhandari *et al.* [13] used the quantum chemical approach complete active space self-consistent field (CASSCF) to calculate the many-body energies of small nanodiamond clusters containing one NV^- center, which are in very good agreement to the experimental results. However, the representation of the bulk defect as defect in a small atomic cluster (around 1 nm in diameter) will only work for very localized defects. Another new method was very recently presented by Ma *et al.* [14] and uses a hybrid density functional theory (DFT) calculation paired with full CI for the active space, just as in the cRPA [12] (or our method), but going beyond the RPA approximation for the screening, yielding good agreement with experiment, but requiring—similarly to cRPA [12]—a computationally very demanding screening.

In this article we present an alternative approach based on a combination of DFT and screened CI that can be used for open shell systems, especially defects in semiconductors as suggested for qubit implementations. It is a semi-empirical approach in the sense that we use a model screening for Coulomb and exchange integrals. Our approach starts from DFT or GW eigenvalues and eigenfunctions. A subset of the electronic system, consisting of the highly correlated electrons, is subsequently used in our screened CI formalism where Coulomb, exchange, and correlations are explicitly (re)calculated. This introduces a double counting which will be accounted for in our approach. Furthermore, a nonlocal screening function is implemented to ensure reduced screening, when the studied system contains vacancies. Without the nonlocal screening function our method is *ab initio* and has no parameters. We apply our methodology to study the electronic structure of the different charge states of the negatively, neutral, and positively charged NV defects. For NV^- and NV^0 a very good agreement between the calculation and experimental findings is obtained. For NV^+ we predict a many-body multiplet structure. ($^1A_1$ - ^3E - ^1E - $^3A_2$ - ^1E) with degeneracy 1-6-2-3-4 and many-body energies with splittings of 1.07-0.24-1.26-0.25 eV.

*gabriel.bester@uni-hamburg.de

II. METHOD

The full CI method is applicable to compute exact solutions to the electronic time-independent Schrödinger equation

$$H|\Psi\rangle = \mathcal{E}|\Psi\rangle. \qquad (1)$$

H is the Hamilton operator, Ψ the many-body wave function, and $\mathcal{E}$ the energy. The "true" molecular electronic Hamiltonian can be written in terms of creation ($a^\dagger$) and annihilation (a) operators in the second quantization formalism

$$H = \underbrace{\sum_{ai} h_{ai} a_a^\dagger a_i}_{A} + \underbrace{\frac{1}{2} \sum_{abji} V_{abji} a_a^\dagger a_b^\dagger a_j a_i}_{B}, \qquad (2)$$

with one and two electron matrix elements

$$h_{ai} = \int \phi_a^*(\boldsymbol{\chi}) \left(-\frac{1}{2}\nabla^2 - \sum_I \frac{Z_I}{r_I} \right) \phi_i(\boldsymbol{\chi}) \, d\boldsymbol{\chi}, \qquad (3)$$

$$V_{abji} = \iint d\boldsymbol{\chi}_1 d\boldsymbol{\chi}_2 \frac{\phi_a^*(\boldsymbol{\chi}_1)\phi_b^*(\boldsymbol{\chi}_2)\,\phi_j(\boldsymbol{\chi}_1)\phi_i(\boldsymbol{\chi}_2)}{r_{12}}, \qquad (4)$$

where Z_I are the nuclear charges, r_I the electron-nuclear separations, r_{12} the electron-electron separation, and $\phi_i(\boldsymbol{\chi})$ the spin orbital, where the coordinates $\boldsymbol{\chi}$ represent collectively the spatial coordinates $\boldsymbol{r}$ and the spin coordinate σ of the electron. The first term of Eq. (2)—the one electron operator—represents the kinetic energy of the electrons and the potential energy arising from the interaction of the electrons with the nuclei. The second term takes the Coulomb interaction between electrons into account.

In the CI approach the many-body wave function $|\Psi\rangle$ is expanded in terms of Slater determinants

$$|\Psi\rangle = c_0|\Psi_0\rangle + \sum_{i,a} c_i^a |\Psi_i^a\rangle + \sum_{\substack{i > j \\ a > b}} c_{ij}^{ab}|\Psi_{ij}^{ab}\rangle + \cdots,$$

where the indices i, j represent occupied orbitals in the reference determinant $|\Psi\rangle$ whereas a, b represent unoccupied (virtual) orbitals. The expansion space is spanned by the reference determinant ($|\Psi_0\rangle$) and by determinants associated with single ($|\Psi_i^a\rangle$), double ($|\Psi_{ij}^{ab}\rangle$), and so on, excitations, where c_0, c_i^a, c_{ij}^{ab}, and so on, are expansion coefficients. Increasing the number of basis states leads to an exponential increase in the number of determinants in CI so that a restricted basis set is necessary [15]. To limit the computational costs Eq. (2) can be split into an active space (as), and a permanently occupied space (core). The division of the active space is shown in Fig. 1. The term A in Eq. (2) can be rewritten as:

$$A = \overbrace{\sum_i^{core} \overbrace{\sum_j^{core}}^{} h_{ij} a_i^\dagger a_j} + \underbrace{\overbrace{\sum_i^{core} \overbrace{\sum_p^{as}}^{} h_{ip} a_i^\dagger a_p}}_{=0, i \text{ is always occupied}}$$

$$+ \underbrace{\overbrace{\sum_p^{as} \overbrace{\sum_i^{core}}^{} h_{pi} a_p^\dagger a_i}}_{=0, i \text{ cannot be changed}} + \overbrace{\sum_p^{as} \overbrace{\sum_q^{as}}^{} h_{pq} a_p^\dagger a_q} \qquad (5)$$

$$= \overbrace{\sum_{ij}^{core} h_{ij} a_i^\dagger a_j} + \overbrace{\sum_{pq}^{as} h_{pq} a_p^\dagger a_q}. \qquad (6)$$
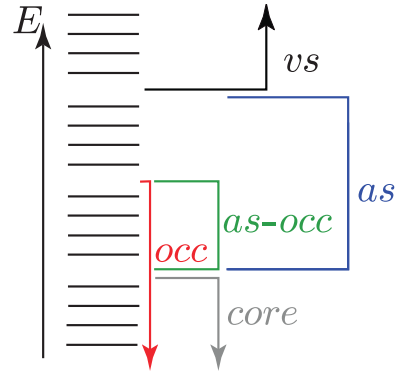

FIG. 1. Schematic illustration of the different subspaces. *occ* describes the occupied states in the ground state. The active space is denoted by *as*. *core* captures all states which are excluded of the active space (*as*) and are therefore permanently occupied. *as-occ* denotes states which are occupied in the ground state and are part of *as*, while *vs* describes the unoccupied virtual space which we neglect in our calculations.

The sums running over as include states in the active space, and sums running over core describe bulk-like states, which are not treated explicitly in our approach. The first term in Eq. (5) is a constant since the core subspace is never changed, and is therefore not considered. The second term in Eq. (5) vanishes because it attempts to create an electron in core, which is always fully occupied. The third term in Eq. (5) vanishes because it would change a core state from occupied to unoccupied, which is forbidden in our restricted space approach.

Applying the same rules to the two body term B [see Eq. (2)] we can simplify the 16 terms to just one (see Supplemental Material [16]). The 15 terms that are neglected in our limited subspace approach can be cast into 11 qualitatively different types of excitations shown in a diagrammatic form in Fig. 2 using full circles for electrons and empty circles for holes. The arrows show the scattering path of the particle (just as in Feynman diagrams [17]). The direct Coulomb terms [Figs. 2(a), 2(f) and 2(l)] and the exchange terms [Figs. 2(d), 2(j) and 2(o)] take a form very similar to the Goldstone
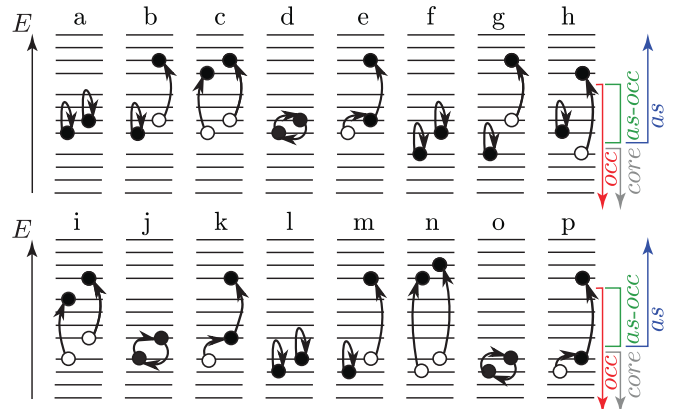

FIG. 2. Illustration of the different terms in part (*B*), (a)–(e) are the considered terms and (f)–(p) are neglected.

diagrams [17] (where in our case the wiggly interaction line is not drawn). Within our restricted space we neglect all excitations corresponding to the diagrams in Figs. 2(f) to 2(p). Neglecting all these diagrams corresponds to the electronic screening of the considered excitations shown in Figs. 2(a) to 2(e), so that we obtain the very simplified expression [18]

$$B = \sum_{pqrs}^{as} V_{pqrs}^{SCR} a_p^\dagger a_q^\dagger a_r a_s. \qquad (7)$$

Substituting A and B by Eq. (6) and Eq. (7) in Eq. (2) yields

$$H = \sum_{pq}^{as} h_{pq} a_p^\dagger a_q + \frac{1}{2} \sum_{pqrs}^{as} V_{pqrs}^{SCR} a_p^\dagger a_q^\dagger a_r a_s . \qquad (8)$$

The second term includes screened integrals

$$V_{pqrs}^{SCR} = \iint d\chi_1 d\chi_2 \, \frac{\phi_p^*(\chi_1)\phi_q^*(\chi_2)\,\phi_r(\chi_1)\phi_s(\chi_2)}{\epsilon(\boldsymbol{r}_1,\boldsymbol{r}_2)|\boldsymbol{r}_1 - \boldsymbol{r}_2|}, \qquad (9)$$

as a consequence of the neglected excitations into and out of the core space, as described above. The screening $\epsilon(\boldsymbol{r}_1,\boldsymbol{r}_2)$ is modeled utilizing a combination of the Resta model [19], expressing the static, isotropic bulk screening of diamond as $\epsilon_{bulk}(|\boldsymbol{r}_1 - \boldsymbol{r}_2|)$. Using this model without any further modifications yields the "unmasked" calculation subsequently described in Fig. 6.

In an attempt to improve the results (we will see later that the improvement is noticeable), at the price of introducing an empirical parameter, we modify the screening in the vicity of the vacancy (slightly reducing it) using a so-called "mask function" $m(r)$ [20,21]:

$$\frac{1}{\epsilon(\boldsymbol{r}_1,\boldsymbol{r}_2)} = 1 + \left(\frac{1}{\epsilon_{bulk}(|\boldsymbol{r}_1 - \boldsymbol{r}_2|)} - 1 \right) m(r_1)m(r_2), \qquad (10)$$

with

$$m(r) = \begin{cases} \frac{1}{2}\left[\left(\cos\left(\frac{r\pi}{2r_{NV}}\right) + 1\right)(\Delta - 1)\right] + 1 & \text{for} \quad r \leqslant 2r_{NV}, \\ 1 & \text{for} \quad r > 2r_{NV}, \end{cases} \qquad (11)$$

with $\Delta < 1$. The mask function $m(r)$ varies smoothly between $m(0) = \Delta$ at the vacancy site ($r = 0$) to a value of one (which means that the full bulk screening is used) at $2r_{NV}$ and beyond, where r_{NV} is the distance from the vacancy to the neighboring nitrogen atom. The screening is therefore reduced in the vicinity of the vacancy using the parameter Δ ($0 < \Delta < 1$). A value of 0.78 was used for Δ in the subsequent work. Whenever the empirical mask function was used in the calculation we use the term "masked results."

The calculation of the screened integrals in Eq. (9) when the nonlocal screening introduced by Eq. (10) is used ("masked results") require three steps: (i) an unmasked unscreened [$\epsilon(\boldsymbol{r}_1,\boldsymbol{r}_2) = 1$]; (ii) a masked [i.e., $m(r)$ is multiplied onto the wave functions] screened [$\epsilon(\boldsymbol{r}_1,\boldsymbol{r}_2) = \epsilon_{bulk}(|\boldsymbol{r}_1 - \boldsymbol{r}_2|)$]; and (iii) a masked unscreened calculation (see the Supplemental Material for further information [16]).

In the following we address the issue of double-counting interactions since we will start from a DFT ground state

that we first partially empty and then repopulate at the CI level. For simplicity we start with the Hartree-Fock (HF) theory, where the Hamiltonian is associated with the Fock operator [18]

$$\hat{F} = \sum_{ij} f_{ij} \, a_i^\dagger a_j$$

$$= \sum_{ij} h_{ij} \, a_i^\dagger a_j + \sum_{ij} \sum_l^{occ} (V_{iljl} - V_{illj}) \, a_i^\dagger a_j \qquad (12)$$

and the Fock matrix elements are given as

$$f_{ij} = h_{ij} + \sum_l^{occ} (V_{iljl} - V_{illj}), \qquad (13)$$

which simplifies in the basis of canonical spin orbitals to [22]

$$f_{ij} = \varepsilon_j^{HF} \delta_{ij}. \qquad (14)$$

Using Eqs. (13) and (14) and the partitioning from Fig. 1, h_{ij} can be written as

$$h_{ij} = \varepsilon_j^{HF} \delta_{ij} - \sum_l^{occ} (V_{iljl} - V_{illj})$$

$$= \varepsilon_j^{HF} \delta_{ij} - \sum_l^{core} (V_{iljl} - V_{illj}) - \sum_l^{as\text{-}occ} (V_{iljl} - V_{illj}), \qquad (15)$$

and the associated one-particle operator is consequently given by

$$\sum_{ij} h_{ij} a_i^\dagger a_j = \sum_{ij}^{core,as} h_{ij} a_i^\dagger a_j = \sum_{ij}^{core,as} \left[\varepsilon_j^{HF} \delta_{ij} \, a_i^\dagger a_j \right.$$

$$- \sum_l^{core} (V_{iljl} - V_{illj}) \, a_i^\dagger a_j$$

$$\left. - \sum_l^{as\text{-}occ} (V_{iljl} - V_{illj}) \, a_i^\dagger a_j \right]. \qquad (16)$$

Similarly to Eq. (2) we completely remove the core part from the equation by introducing a screening on the remaining integrals

$$\sum_{pq}^{as} h_{pq} a_p^\dagger a_q = \sum_{pq}^{as} \left(\varepsilon_q^{HF} \delta_{pq} \, a_p^\dagger a_q \right.$$

$$\left. - \sum_s^{as\text{-}occ} \left(V_{psqs}^{SCR} - V_{pssq}^{SCR} \right) a_p^\dagger a_q \right). \qquad (17)$$

Rewriting Eq. (8) using Eq. (17) we obtain

$$H = \sum_{pq}^{as} \left[\varepsilon_p^{HF} \delta_{pq} - \sum_s^{as\text{-}occ} \left(V_{psqs}^{SCR} - V_{pssq}^{SCR} \right) \right] a_p^\dagger a_q$$

$$+ \frac{1}{2} \sum_{pqrs}^{as} V_{pqrs}^{SCR} a_p^\dagger a_q^\dagger a_r a_s. \qquad (18)$$

Equation (18) can be rewritten as

$$H = \sum_p^{as} \varepsilon_p^{eff} a_p^\dagger a_p - \sum_{p \neq q}^{as} \sum_s^{as-occ} \left(V_{psqs}^{SCR} - V_{pssq}^{SCR} \right) a_p^\dagger a_q$$
$$+ \frac{1}{2} \sum_{pqrs}^{as} V_{pqrs}^{SCR} a_p^\dagger a_q^\dagger a_r a_s, \tag{19}$$

where an effective eigenvalue has been introduced:

$$\varepsilon_p^{eff} = \varepsilon_p^{HF} - \sum_s^{as-occ} \left(V_{psps}^{SCR} - V_{pssp}^{SCR} \right), \tag{20}$$

and V_{psps}^{SCR} are Coulomb and V_{pssp}^{SCR} exchange screened integrals. With this approach we explicitly eliminate the double counting of the Coulomb and exchange integrals and only the correlation in the active space already included in DFT/GW is calculated twice and are not explicitly removed.

An issue arises from partially occupied degenerate states in the reference Slater determinant. For a set of m degenerate states occupied by n electrons, the effective eigenvalues ε_p^{eff} are given by the HF eigenvalues ε_p^{HF} corrected by the sum given in Eq. (20). This correction is different for the occupied and for the unoccupied states introducing an artificial breaking of the degeneracy. To circumvent this problem, we use the same fractional occupation $c_l = n/m$ for all the degenerate states. For the eigenvalue ε_p^{HF} we use the best available quasiparticle eigenvalues. In the NV case presented subsequently, we use GW, where we expect an accuracy in the 0.1-eV range. For larger systems, either experimental values, or from high-level DFT (e.g., hybrid functionals), or from semi-empirical approaches such as atomic effective pseudopotentials (AEP) [23] can be used:

$$\epsilon_p^{eff} = \epsilon_p^{GW,DFT,AEP} - \sum_s^{as-occ} c_s \left(V_{psps}^{SCR} - V_{pssp}^{SCR} \right) \tag{21}$$

and accordingly,

$$H = \sum_p^{as} \epsilon_p^{eff} a_p^\dagger a_p - \sum_{p \neq q}^{as} \sum_s^{as-occ} c_s \left(V_{psqs}^{SCR} - V_{pssq}^{SCR} \right) a_p^\dagger a_q$$
$$+ \frac{1}{2} \sum_{pqrs}^{as} V_{pqrs}^{SCR} a_p^\dagger a_q^\dagger a_r a_s. \tag{22}$$

We explicitly perform spin-unpolarized calculations since spin-polarized DFT calculations using a local density functional (SLDA), similar to unrestricted HF, result in wave functions represented by a single determinant and are therefore not pure spin states, i.e., the wave functions are not eigenfunctions of the total spin operator $\hat{S}^2$. SLDA leads to different spatial distributions for spins of opposite signs and hence a spin dependence in the Coulomb integrals. As an example, the net spin $S = +1$ state of the NV$^-$ system should be entirely identical to the state with $S = -1$, however, in SLDA one configuration is chosen arbitrarily and the majority spin eigenvalues are shifted lower in energy. In other words, the Coulomb integrals become irreparably spin-dependent. To preserve the equivalence of these two configurations, both the eigenvalues and eigenfunctions must be entirely spin-degenerate, i.e., spin-unpolarized calculations must be carried out. Hence, our approach is based on ground-state calculations within LDA instead of SLDA or spin-unpolarized GW. All calculations were performed at the spin triplet ground-state geometries, which yields vertical excitation energies [equal to the sum of zero phonon line (ZPL) and excited state Stokes energies].

III. COMPUTATIONAL DETAILS

All calculations were performed with the ABINIT [24] software package. For the DFT calculations the Brillouin zone is sampled at the Γ point and a kinetic energy cutoff of $E_c = 35$ Hartree is used. A Troullier-Martins norm-conserving pseudopotential is used with $l_{max} = 1$ and $l_{loc} = 1$ for carbon as well as for nitrogen. To obtain the NV center orbitals the calculations were performed at the LDA level on 511 atom supercells with periodic boundary conditions; fractional occupation was used and the structures fully relaxed. The GW calculations were performed with a 215 atom supercell with a cutoff of $E_c = 15$ Hartree. The plasmon-pole model is applied with 768 empty bands.

IV. SINGLE-PARTICLE RESULTS

We study the NV center in the three existing [25–29] charged states NV$^-$, NV^0, and NV$^+$. Calculations performed at the LDA level on 511 and 215 atom supercells and fully relaxed structures reveal that the single-particle energies are converged to within 5 meV already in the smaller supercell (see Supplemental Material [16] and note that the wave functions require the larger supercells for convergence). This reduction of supercell size allows us to base the quasiparticle energy part of our screened-CI calculations on results obtained at the more accurate GW level. This is a rather fortunate situation where GW is affordable; for more delocalized defects requiring larger supercells the use of more empirical eigenvalues (corrected AEP or extracted from experiment) would be necessary.

The quasiparticle GW eigenvalues along with the bulk diamond conduction band minimum (CBM) and valence band maximum (VBM) are shown in Fig. 3. The defect related band-gap states a_1 and $e_{x,y}$ have different occupations depending on the charge of the defect center. For the NV$^-$ defect center six electrons are involved: three from the three neighboring carbon atoms, two from the nitrogen dangling bond, and one captured from the lattice. Two of them occupy the $a_1(1)$ state laying energetically below the VBM and not shown in Fig. 3. We consider this state in our calculations, but adding it to the active space in the CI changes the many-body energy for NV$^-$ by less then 60 meV. For the NV^0 and NV$^+$ center the change is below 10 meV. The six electrons occupy the $a_1(1)$, $a_1(2)$, and $e_{x,y}$ states. In the NV$^-$, NV^0, and NV$^+$ cases only four, three, and two electrons occupy the band-gap defect states, respectively. A clear shift of band-gap states towards the VBM is observed by removing electrons going from NV$^-$ to the NV$^+$ system as shown in Fig. 3. The splittings between the VBM and the $a_1(2)$ states are 0.92 eV (NV$^-$), 0.64 eV (NV^0), and 0.51 eV (NV$^+$) while the energy differences between the two gap states $a_1(2)$ and $e_{x,y}$ are 2.09 eV, 1.86 eV, and 1.61 eV, respectively.
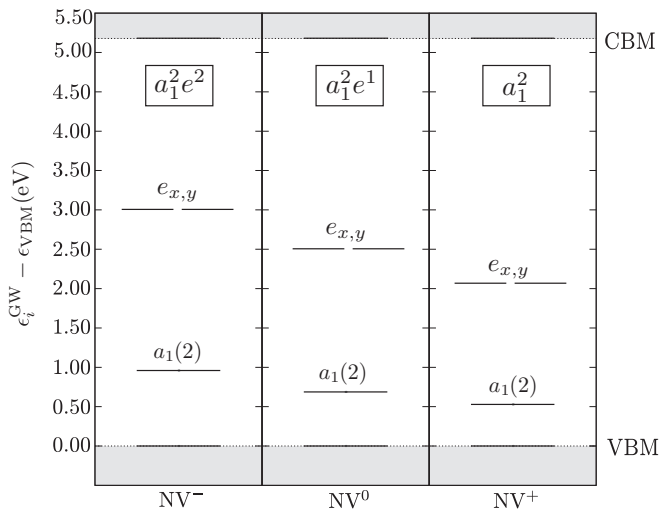
FIG. 3. Quasiparticle eigenvalues of bulk diamond (215 atom supercell) with an embedded negatively, neutral, and positively charged NV center (NV$^{-/0/+}$) calculated within GW. All eigenvalues are aligned to the VBM. The $a_1(1)$ defect state is not shown and below the VBM, but taken into account in our active CI space.

To illustrate the localization of the state $a_1(1)$ we plot in Fig. 4 the square of the wave function as a yellow isosurface and notice the rather localized character with strongest contribution around the nitrogen atom. On the lower panel of Fig. 5 a one-dimensional representation of the single-particle wave functions of the $a_1(2)$ (yellow), the $a_1(1)$ (blue), and the $e_{x,y}$ (green) states is shown, along with the delocalized VBM state (black dashed) and an artificial constant charge background (purple), for comparison. Compared to the delocalized states (black and purple), the defect states are highly localized around the vacancy. We use this localization description to illustrate our mask function $m(r)$ introduced in Eq. (11) on the upper panel of Fig. 5. When using our empirical screening reduction ("masked results") we therefore reduce the screening by about 15% in the region of space where the localized states reside.
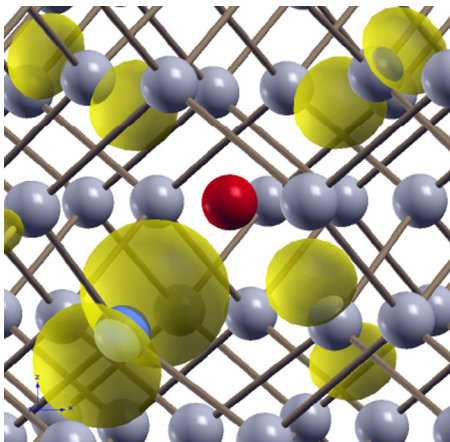

FIG. 4. Electron density (yellow) for the defect state $a_1(1)$ of the NV$^-$ defect laying energetically in the valence band. The nitrogen, carbon, and vacancy are shown in blue, grey, and red, respectively.
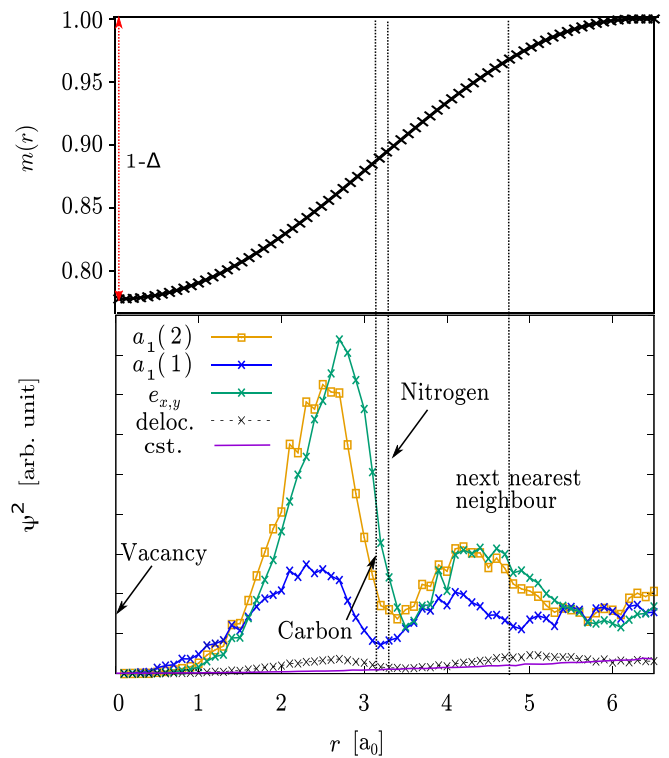

FIG. 5. Upper panel: Plot of the mask function $m(r)$ as a function of the distance from the vacancy. Lower panel: One-dimensional plots of different single particle states of the NV$^-$ defect: $a_1(2)$ is shown in yellow, $a_1(1)$ in blue, $e_{x,y}$ in green, a delocalized state from the valence band states in black, and a constant wave function (purple) for comparison. The dashed vertical lines show the distance from the vacancy to the nearest-neighbor nitrogen and carbon atoms as well as to the second, nearest-neighbor carbon.

Note that while the use of GW quasiparticle energies was possible and meaningful using the smaller supercell of 215 atoms, the Coulomb and exchange integrals must be calculated using wave functions obtained for the larger 511 atom supercell. Indeed, using wave functions from the smaller 215 atom supercell leads to errors in the many-body energies in the order of 200 meV (see Supplemental Material [16]).

V. MANY-BODY RESULTS OF THE NV$^-$ DEFECT

Since the NV$^-$ defect has been thoroughly investigated theoretically and experimentally this gives us the opportunity to use it as benchmark system. In Fig. 6 we show an extensive comparison to experiment and other calculations. The photoexcited states are shown in blue while the states before excitation are shown in black. Figures 6(a) to 6(h) show theoretical results obtained by various approaches as described subsequently and in the figure caption. The length of the arrows corresponds to the experimental results, as described next.

We start by comparing our unmasked [Fig. 6(a)] and masked results [Fig. 6(b)] to the experimental data. Davies *et al.* measured a vertical excitation energy (VEE) of 2.2 eV [30]. Our unmasked result overestimate this splitting by about 70 meV and our masked result is within excellent agreement
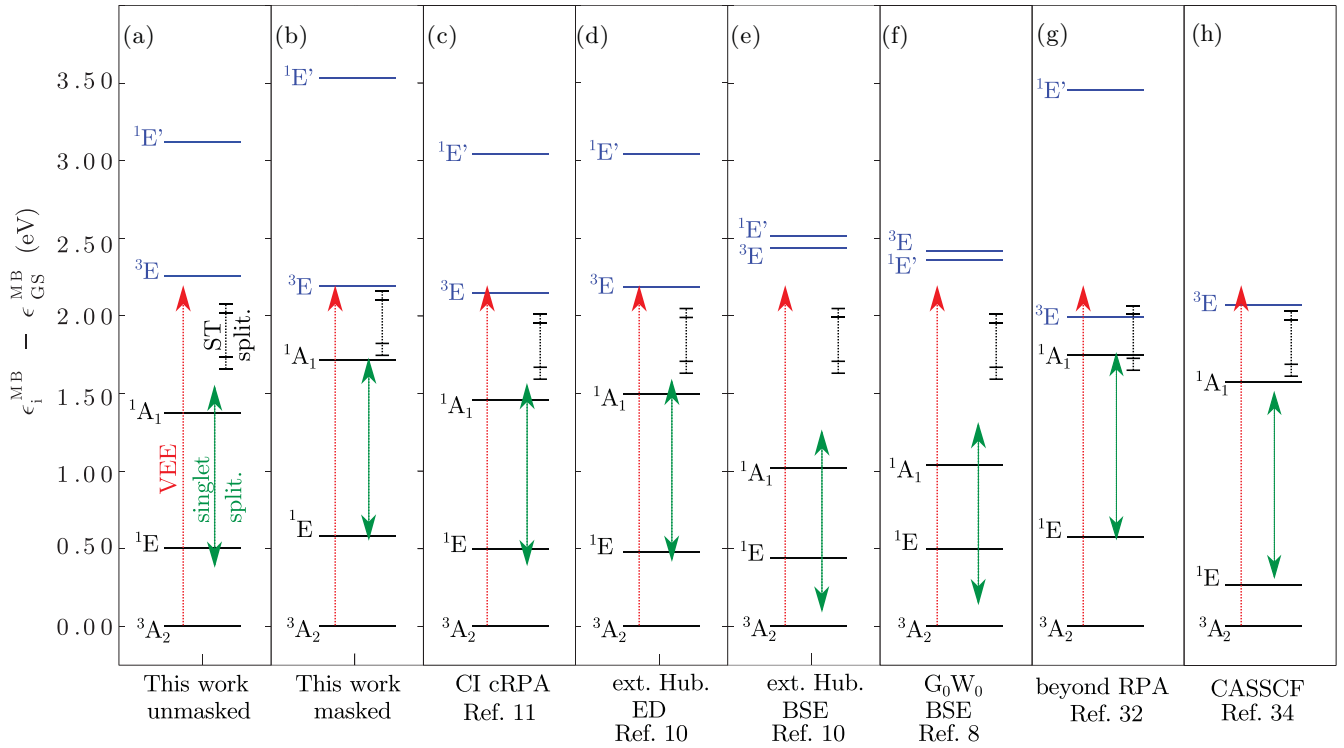
FIG. 6. Comparison of the many-body energies of NV^- calculated with different approaches. Photoexcited states are shown in blue. Experimental known values of the vertical excitation (VEE) are shown as red arrows [30], the singlet state splitting (singlet split.) is shown as green arrows [31], and the singlet-triplet splitting (ST split.) is shown as black line with error bars [32,33]. (a) Our "*ab initio*" results without modifying the screening in the vicinity of the vacancy (unmasked). (b) Our results using a mask function $m(r)$ with $\Delta = 0.78$. (c) CI-constrained RPA results of Ref. [12]. (d) Extended Hubbard model fitted to GW calculations solved using exact diagonalization, taken from Ref. [10]. (e) Extended Hubbard model fitted to GW calculations with BSE Ref. [10]. (f) G_0W_0-BSE results taken from Ref. [8]. (g) Beyond-RPA (hybrid DFT coupled with Full CI) from Ref. [14]. (h) CASSCF calculation of a 162 Atom cluster from Ref. [13].

with this experiment. Our calculations reveal that the VEE is a poor indicator of the quality of the correlated calculations. Indeed, applying no screening at all changes the VEE by only 30 meV, while the integrals and the splittings between the black and the blue states change by up to a factor of 2. The VEE is mainly a direct consequence of the quasiparticle energies (GW in our case).

Another experimentally known quantity is the singlet-triplet splitting $(^3E - {}^1A_1)$ as measured by Goldman *et al.* [32–34]. A combination of experiment and simple model lead to singlet-triplet splitting $(^3E - {}^1A_1)$ in a region between 340 to 430 meV. The black dashed line with the two black bars represent the 340 and 430 meV splittings in Fig. 6 and is placed in the figure in such a way as to ease the comparison to the theoretical results. Our masked result is in good agreement with this experiment and our unmasked result overestimates this splitting by 460 meV.

The third experimental results on the NV^- system is the singlet splitting measured by Rogers *et al.* [31]. Using a magnetic field and uniaxial stress a $^1E - {}^1A_1$ splitting of 1190 meV (singlet split) could be determined. Our masked result is again in good agreement with this experiment and our unmasked result underestimates this splitting by 320 meV.

We pursue by a comparison to other calculations. The calculations of Figs. 6(c) [12] and 6(d) [10] overestimate the singlet-triplet and underestimate the singlet splitting. Both

approaches have very good quasiparticle energies and calculate a VEE with excellent agreement to the experiment. The $^3A_2$ - ^1E and ^1E - $^1A_1$ splittings of Figs. 6(c) and 6(d) are very similar to our unmasked results of Fig. 6(a). The results of beyond-RPA [Fig. 6(g)] [14] underestimates the VEE by about 0.2 eV due to a different set of quasiparticle energies. However, their use of an improved screening yields a singlet-triplet and singlet splitting in excellent agreement with the experiment. The recent work of Bhandari *et al.* [Fig. 6(h)] using CASSCF on very small clusters, show excellent agreement for all the known quantities. The GW + BSE calculations of the authors of Refs. [8,10] show a very poor agreement with the experiment since the electron hole picture used in the BSE formalism forces the selection of a single ground-state determinant on which all single-electron-hole excitations are constructed, yielding an incomplete description. This was already recognized and described by Choi *et al.* [10].

Our screened CI formalism allows for an analysis of our many-body states in terms of the importance of certain configurations. The results are presented in Table I where the many-body character is described in terms of the percentage of the different constituting configurations. The $a_1(2)$ state is numbered "1," $e_{x,y}$ are numbered "2" and "3." The overbared (bare) numbers mark spin-down (spin-up) electrons. The $a_1(1)$ state is not shown since it is fully occupied

TABLE I. The electronic dominant configurations (Config.), the many-body states (MB), the many-body state index, and the character of the corresponding wave functions of the NV⁻ defect are given. The a_1 state is numbered "1," $e_{x,y}$ are numbered "2" and "3." The overbared (bare) numbers mark spin-down (spin-up) electrons. Configurations with a weight below one percent are not shown.

Config.	MB	Index	Wave function
	$^3A_2$	1	$100\%\lvert 1\bar{1}23\rangle$
		2	$50\%\lvert 1\bar{1}2\bar{3}\rangle + 50\%\lvert 1\bar{1}\bar{2}3\rangle$
		3	$100\%\lvert 1\bar{1}\bar{2}\bar{3}\rangle$
$a_1^2 e^2$	^1E	1	$32\%\lvert 1\bar{1}\bar{2}3\rangle + 32\%\lvert 1\bar{1}2\bar{3}\rangle + 12\%\lvert 1\bar{1}3\bar{3}\rangle$
			$12\%\lvert 1\bar{1}2\bar{2}\rangle + 6\%\lvert \bar{1}2\bar{3}3\rangle + 6\%\lvert 1\bar{2}3\bar{3}\rangle$
		2	$32\%\lvert 1\bar{1}3\bar{3}\rangle + 32\%\lvert 1\bar{1}2\bar{2}\rangle + 12\%\lvert 1\bar{1}\bar{2}3\rangle$
			$12\%\lvert 1\bar{1}2\bar{3}\rangle + 6\%\lvert \bar{1}2\bar{2}3\rangle + 6\%\lvert 12\bar{2}\bar{3}\rangle$
	$^1A_1$	1	$48\%\lvert 1\bar{1}3\bar{3}\rangle + 48\%\lvert 1\bar{1}2\bar{2}\rangle + 3\%\lvert 2\bar{2}3\bar{3}\rangle$
	^3E	1	$66\%\lvert 12\bar{2}3\rangle + 32\%\lvert 123\bar{3}\rangle$
		2	$65\%\lvert \bar{1}2\bar{2}3\rangle + 27\%\lvert \bar{1}2\bar{3}3\rangle + 6\%\lvert 12\bar{2}\bar{3}\rangle$
			$6\%\lvert \bar{1}2\bar{2}3\rangle$
		3	$27\%\lvert \bar{1}2\bar{2}3\rangle + 17\%\lvert 12\bar{2}\bar{3}\rangle + 17\%\lvert \bar{1}2\bar{3}3\rangle$
			$13\%\lvert \bar{1}2\bar{3}3\rangle + 8\%\lvert \bar{1}2\bar{2}3\rangle + 8\%\lvert 123\bar{3}\rangle$
		4	$61\%\lvert 123\bar{3}\rangle + 39\%\lvert 12\bar{2}3\rangle$
$a_1^1 e^3$		5	$26\%\lvert \bar{1}233\rangle + 26\%\lvert 1\bar{2}33\rangle + 17\%\lvert \bar{1}2\bar{2}3\rangle$
			$17\%\lvert 12\bar{2}3\rangle + 8\%\lvert 123\bar{3}\rangle + 6\%\lvert \bar{1}233\rangle$
		6	$53\%\lvert \bar{1}2\bar{3}3\rangle + 33\%\lvert \bar{1}2\bar{2}3\rangle + 4\%\lvert \bar{1}2\bar{3}3\rangle$
			$4\%\lvert 12\bar{3}3\rangle + 3\%\lvert 12\bar{2}3\rangle + 3\%\lvert \bar{1}2\bar{2}3\rangle$
	$^1E'$	1	$31\%\lvert \bar{1}2\bar{2}3\rangle + 31\%\lvert 12\bar{2}\bar{3}\rangle + 13\%\lvert \bar{1}2\bar{3}3\rangle$
			$13\%\lvert \bar{1}2\bar{3}3\rangle + 6\%\lvert 1\bar{1}23\rangle + 6\%\lvert 1\bar{1}\bar{2}3\rangle$
		2	$31\%\lvert 12\bar{3}3\rangle + 31\%\lvert 1\bar{2}3\bar{3}\rangle + 13\%\lvert 12\bar{2}\bar{3}\rangle$
			$13\%\lvert 1\bar{2}\bar{2}3\rangle + 6\%\lvert 1\bar{1}3\bar{3}\rangle + 6\%\lvert 1\bar{1}2\bar{2}\rangle$

FIG. 7. Screened CI many-body energies for NV$^{-/0/+}$. Photoexcited states are shown in blue. The experimentally known quantities are shown as arrows. The black dashed arrow means that the transition is optically dark.

in every configuration Our calculations reveal, for instance, that the ground state ($^3A_2$) consists of Slater determinants all belonging to the $a_1^2 e^2$ configuration, while the ^1E state shows a 14% contribution from Slater determinants of the excited sates configuration $a_1^1 e^3$ (namely $\lvert \bar{1}23\bar{3}\rangle$ and $\lvert 1\bar{2}3\bar{3}\rangle$ for state index (1). The corresponding results for NV^0 and NV$^+$ are shown in the Supplemental Material [16].

VI. MANY-BODY RESULTS OF THE NV^0 AND NV$^+$ DEFECTS

Now that we established the quality of the approach, we show in Fig. 7 our screened CI many-body energies for all three charge states of the NV center. Our results for NV$^-$ already discussed in detail are repeated here on the left panel for comparison. For NV^0 we obtain the sequence of many-body sates ^2E - $^4A_2$ - $^2A_2$ - ^2E - $^2A_1$ shown in Fig. 7 with respective degeneracies 4-4-2-4-2. The splitting between the states are 0.68-0.97-0.39-0.89 eV, which corresponds to a first optically allowed transition from ^2E to the $^2A_2$ state at 1.65 eV compared to the experimental VEE of 2.156 eV (575 nm) [35,36]. As described already for the NV$^-$ defect, the VEE is very sensitive to the single-particle splitting of the band-gap states a_1 and $e_{x,y}$ and show only a weak dependence on the screening and quality of the integrals. Note that the NV^0 ground state is a Jahn-Teller distorted state and the $e_{x,y}$ states are split by 90 meV [37]. However, this rather small splitting cannot bring the theoretical results in agreement with experiment.
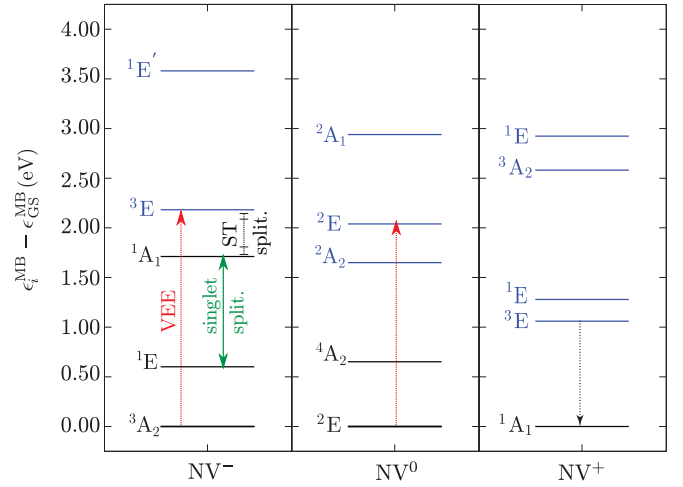
Indeed, to reproduce the experimental VEE, a quasiparticle energy splitting of 2.55 eV would be required instead of the 1.86 eV result from GW. Our discrepancy with the experiment therefore originates mainly from a poor single-particle description at the GW (and LDA) level: the NV^0 ground state, with its open-shell character, is only poorly represented by a single determinant approach such as GW or LDA. Other theoretical studies suggest a different many-electron energy ordering; Ranjbar *et al.* [38] calculated ^2E - $^4A_2$ - $^2A_1$ - ^2E - $^2A_1$ with a vertical excitation energy of 2.64 eV, based on a Hubbard Hamiltonian for small carbon clusters. Zyubin *et al.* [39] obtained ^2E - $^2A_2$ - ^2E - $^2A_1$ - ^2E with optical excitation of 2.4 eV, based on a CASSCF calculation of the ground state (circumventing the GW and LDA shortcomings) and CASPT2 for the excited states, but also only for very small carbon clusters.

For the NV$^+$ charged defect we obtain the sequence $^1A_1$ - ^3E - ^1E - $^3A_2$ - ^1E with the respective degeneracies 1-6-2-3-2. The many-body energy splitting are 1.071-0.235-1.515-0.98 eV. For the NV$^+$ system no fluorescence is observed experimentally [28] in qualitative agreement with our result of a triplet lowest-energy excited state. An analysis of the many-body states (as shown in Table I but for NV$^+$, shown in the Supplemental Material [16]) reveals that the ground state ($^1A_1$) is constituted solely by the configuration $a_1^2 e^0$. Similarly, the six-fold multiplet (^3E) consists only of Slater determinants derived from the $a_1^1 e^1$ configuration, while the ^1E state includes 4% of Slater determinants derived from the doubly excited configuration ($a_1^0 e^2$).

Finally, note that the results presented here where obtained for a CI basis containing Slater determinants built from the four defect states $a_1(1)$, $a_1(2)$, $e_{x,y}$. Expanding the CI basis by Slater determinants including additional single-particle states lying energetically in the VB shows very little influence. For example, in the NV$^-$ case using Slater determinants with an additional four states of the VB lead to a vertical excitation shift of six meV. Adding four CB states shifts the excitation

by two meV. The NV^0 and NV$^+$ defects behave very similarly with respect to CI convergence.

VII. SUMMARY

In summary, we present a computational method to calculate the correlated many-body multiplet levels typically originating from atomic defects in semiconductors used in the context of quantum information (qubits). The method includes the static correlations among the localized defect states, which is often inaccurately described at the level of GW and BSE. The advantage of our method is the low computational demand, which does not exceed a typical *ab initio* DFT calculation. We base our method on a highly correlated subspace of the localized defect states embedded in an environment of bulk-like delocalized electrons, in a similar spirit as in the dynamical mean-field theory [11,40]. The dielectric environment is modeled by a semi-empirical microscopic screening function and the many-body Hamiltonian is solved using a full configuration interaction approach with screened Coulomb and exchange integrals. For the screening we used either a microscopic Thomas-Fermi-like model derived from bulk diamond or an empirically modified version of the latter where screening is slightly reduced in the vicinity of the vacancy. We illustrate the capability of the method by applying it to the different charged states of the NV center in diamond. For this quite strongly localized defect, the quasiparticle levels entering our screened-CI approach are obtained from many-body perturbation theory within the GW approach. For other, less localized defects, the use of GW would be prohibitive and the quasiparticle energies could be taken from experiment or from semi-empirical approaches such as atomic effective pseudopotentials [41–43], which would allow to calculate systems with tens of thousands of atoms [42]. For the extensively studied system NV$^-$, we obtain the sequence of states $^3A_2$ - ^1E - $^1A_1$ - ^3E - $^1E'$ with energy splitting of 0.58-1.14-0.48-1.27 eV in excellent agreement with the experiment. For NV^0 we obtain the sequence ^2E - $^4A_2$ - $^2A_2$ - ^2E - $^2A_1$ with respective splittings 0.68-0.97-0.39-0.89 eV, corresponding to an underestimated transition energy (theory: 1.62 eV, experiment: 2.156 eV). We attribute the main part of this discrepancy to the inaccuracy of the GW result, which is expected since the ground state is an open-shell system. For the NV$^+$ charged defect we obtain the sequence $^1A_1$ - ^3E - ^1E - $^3A_2$ - ^1E with splitting of 1.07-0.24-1.26-0.25 eV, which agrees with the experiment in the sense that no emission is observed experimentally, and we obtain a dipole forbidden lowest-energy transition.

[1] T. Staudacher, F. Shi, S. Pezzagna, J. Meijer, J. Du, C. A. Meriles, F. Reinhard, and J. Wrachtrup, Nuclear magnetic resonance spectroscopy on a (5-nanometer)^3 sample volume, Science **339**, 561 (2013).

[2] F. Shi, Q. Zhang, P. I. Wang, H. Sun, J. Wang, X. Rong, M. Chen, C. Ju, F. Reinhard, and H. Chen, Single-protein spin resonance spectroscopy under ambient conditions, Science **347**, 1135 (2015).

[3] F. Dolde, M. W. Doherty, J. Michl, I. R Jakobi, B. Naydenov, S. Pezzagna, J. Meijer, P. Neumann, F. Jelezko, N. B. Manson, and J. Wrachtrup, Nanoscale Detection of A Single Fundamental Charge in Ambient Conditions using the *NV*$^-$ Center in Diamond, Phys. Rev. Lett. **112**, 097603 (2014).

[4] Y. Wu, Y. Wang, X. Qin, X. Rong, and J. Du, A programmable two-qubit solid state quantum processor under ambient conditions, npj Quantum Inf. **5**, 9 (2019).

[5] L. C. Bassett, A. Alkauskas, A. L. Exarhos, and K. M. C. Fu, Quantum defects by design, Nanophotonics **8**, 1867 (2020).

[6] P. Neumann, I. Jakobi, F. Dolde, C. Burk, R. Reuter, G. Waldherr, J. Honert, T. Wolf, A. Brunner, and J. H. Shim, High-precision nanoscale temperature sensing using single defects in diamond, Nano Lett. **13**, 2738 (2013).

[7] G. Kucsko, P. C. Maurer, N. Y. Yao, M. Kubo, H. J. Noh, P. K. Lo, H. Park, and M. D. Lukin, Nanometre-scale thermometry in a living cell, Nature (London) **500**, 54 (2013).

[8] Y. Ma, M. Rohlfing, and A. Gali, Excited states of the negatively charged nitrogen-vacancy color center in diamond, Phys. Rev. B **81**, 041204(R) (2010).

[9] L. Hung, F. H. da Jornada, J. Souto-Casares, J. R. Chelikowsky, S. G. Louie, and S. Öğüt, Excitation spectra of aromatic molecules within a real-space GW-BSE formalism: Role of self-consistency and vertex corrections, Phys. Rev. B **94**, 085125 (2016).

[10] S. K. Choi, M. Jain, and S. G. Louie, Mechanism for optical initialization of spin in NV$^-$ center in diamond, Phys. Rev. B **86**, 041202(R) (2012).

[11] D. Zgid, E. Gull, and G. K.-L. Chan, Truncated configuration interaction expansion as solvers for correlated quantum impurity models and dynamical mean-field theory, Phys. Rev. B **86**, 165128 (2012).

[12] M. Bockstedte, F. Schütz, T. Garatt, V. Ivàdy, and A. Gali, *Ab initio* description of highly correlated states in defects for realizing quantum bits, Quantum Mater. **3**, 31 (2018).

[13] C. Bhandari, A. Wysocki, S. E. Economou, P. Dev, and K. Park, A multiconfigurational study of the negatively charged nitrogen-vacancy center in diamond, Phys. Rev. B **103**, 014115 (2021).

[14] H. Ma, M. Govoni, and G. Galli, Quantum simulations of materials on near-term quantum computers, NPJ Comput. Mater. **6**, 85 (2020).

[15] F. Jensen, *Introduction to Computational Chemistry*, 2nd ed., (John Wiley & Sons, London, 2007).

[16] See Supplemental Material at http://link.aps.org/supplemental/10.1103/PhysRevB.104.104105 for additional information supporting the derivation of the various equations and the different convergence tests performed on the numerical results.

[17] A. L. Fetter J. D. Walecka, *Quantum Theory of Many-Particle Systems*, 1st ed. (Mcgraw-Hill, New York, 1971).

[18] Denis Antonov, Investigations on diamond structures with embedded defects centres using numerical and ab initio simulation techniques, Ph.D. thesis, University of Stuttgart, 2017.

[19] R. Resta, Thomas-Fermi dielectric screening in semiconductors, Phys. Rev. B **16**, 2717 (1977).

[20] X. Cartoixà and L. W. Wang, Microscopic Dielectric Response Functions in Semiconductor Quantum Dots, Phys. Rev. Lett. **94**, 236804 (2005).

[21] L. W. Wang, M. Califano, A. Zunger, and A. Franceschetti, Pseudopotential Theory of Auger Processes in CdSe Quantum Dots, Phys. Rev. Lett. **91**, 056404 (2003).

[22] T. Helgaker, P. Jorgensen, and J. Olsen, *Molecular Electronic-Structure Theory*, 1st ed. (John Wiley & Sons, London, 2000).

[23] J. R. Cárdenas and G. Bester, Atomic effective pseudopotentials for semiconductors, Phys. Rev. B **86**, 115332 (2012).

[24] X. Gonze G. B. Amadon P. M. Anglade J. M. Beuken F. Bottin P. Boulanger F. Bruneval D. Caliste R. Caracas T. Deutsch, and L. Genovese, ABINIT: First-principles approach to material and nanosystem properties, Comput. Phys. Commun. **180**, 12 (2009).

[25] M. V. Hauf, B. Grotz, B. Naydenov, M. Dankerl, S. Pezzagna, J. Meijer, F. Jelezko, J. Wrachtrup, M. Stutzmann, F. Reinhard, and J. A. Garrido, Chemical control of the charge state of nitrogen-vacancy centers in diamond, Phys. Rev. B **83**, 081304(R) (2011).

[26] B. Grotz, M. V. Hauf, M. Dankerl, B. Naydenov, S. Pezzagna, J. Meijer, F. Jelezko, J. Wrachtrup, M. Stutzmann, and F. Reinhard, Charge state manipulation of qubits in diamond, Nat. Commun. **3**, 729 (2012).

[27] M. V. Hauf, P. Simon, N. Aslam, M. Pfender, P. Neumann, S. Pezzagna, J. Meijer, J. Wrachtrup, M. Stutzmann, and F. Reinhard, Addressing single nitrogen-vacancy centers in diamond with transparent in-plane gate structures, Nano Lett. **14**, 2359 (2014).

[28] C. Schreyvogel, V. Polyakov, R. Wunderlich, J. Meijer, and C. E. Nebel, Active charge state control of single NV centres in diamond by in-plane Al-Schottky junctions, Sci. Rep. **5**, 12160 (2015).

[29] A. Lenef and S. C. Rand, Electronic structure of the N-V center in diamond: Theory, Phys. Rev. B **53**, 13441 (1996).

[30] G. Davies and M. F. Hamer, Optical studies of the 1.945 eV vibronic band in diamond, Proc. R. Soc. London A **348**, 285 (1976).

[31] L. J. Rogers, S. Armstrong, M. J. Sellars, and N. B. Manson, Infrared emission of the NV centre in diamond: Zeeman and uniaxial stress studies, New J. Phys. **10**, 103024 (2008).

[32] M. L. Goldman, A. Sipahigil, M. W. Doherty, N. Y. Yao, S. D. Bennet, M. Markham, D. J. Twitchen, N. B. Manson, A. Kubanek, and M. D. Lukin, Phonon-Induced Population Dynamics and Intersystem Crossing in Nitrogen-Vacancy Centers, Phys. Rev. Lett. **114**, 145502 (2015).

[33] A. Gali, *Ab initio* theory of the nitrogen-vacancy center in diamond, Nanophotonics **8**, 1907 (2019).

[34] A. Drabenstedt, L. Fleury, C. Tietz, F. Jelezko, S. Kilin, A. Nizovtzev, and J. Wrachtrup, Low-temperature microscopy and spectroscopy on single defect centers in diamond, Phys. Rev. B **60**, 11503 (1999).

[35] G. Davies, Dynamic Jahn-Teller distortions at trigonal optical centres in diamond, J. Phys. C: Solid State Phys. **12**, 2551 (1979).

[36] N. B. Manson, K. Beha, A. Batalov, L. J. Rogers, M. W. Doherty, R. Bratschitsch, and A. Leitenstorfer, Assignment of the NV^0 575-nm zero-phonon line in diamond to a ^2E - $^2A_2$ transition, Phys. Rev. B **87**, 155209 (2013).

[37] A. Gali, Theory of the neutral nitrogen-vacancy center in diamond and its application to the realization of a qubit, Phys. Rev. B **79**, 235210 (2009).

[38] A. Ranjbar, M. Babamoradi, M. Heidari Saani, M. A. Vesaghi, K. Esfarjani, and Y. Kawazoe, Many-electron states of nitrogen-vacancy centers in diamond and spin density calculations, Phys. Rev. B **84**, 165212 (2011).

[39] A. S. Zyubin, A. M. Mebel, M. Hayashi, H. C Chang, and S. H. Lin, Quantum chemical modeling of photoabsorption properties of the nitrogen-vacancy point defect in diamonds, J. Comput. Chem. **30**, 119 (2009).

[40] A. Georges, G. Kotliar, W. Krauth, and M. J. Rozenberg, Dynamical mean-field theory of strongly correlated fermion systems and the limit of infinite dimensions, Rev. Mod. Phys. **68**, 13 (1996).

[41] G. Bester, Electronic excitations in nanostructures: an empirical pseudopotential based approach, J. Phys.: Condens. Matter. **21**, 023202 (2008).

[42] F. Zirkelbach, P.-Y. Prodhomme, P. Han, R. Cherian, and G. Bester, Large-scale atomic effective pseudopotential program including an efficient spin-orbit coupling treatment in real space, Phys. Rev. B **91**, 075119 (2015).

[43] A. Karpulevich, H. Bui, D. Antonov, P. Han, and G. Bester, Nonspherical atomic effective pseudopotentials for surface passivation, Phys. Rev. B **94**, 205417 (2016).